Quantitative Photo-Acoustic Imaging based on data normalisation : application to the reconstruction of the opto-mechanical properties of the intervertebral disc

Antoine Capart, Roman Allais, Julien Wojak, Olivier Boiron, Anabela Da Silva

Quantitative Photo-Acoustic Imaging based on data normalisation : application to the reconstruction of the opto-mechanical properties of the intervertebral disc

Antoine Capart, Roman Allais, Julien Wojak, Olivier Boiron, and Anabela Da Silva

Aix Marseille Univ, CNRS, Centrale Med, Institut Fresnel, Marseille, France
Aix Marseille Univ, CNRS, Centrale Med, IRPHE, Marseille, France

E-mail: anabela.dasilva@fresnel.fr

septembre 2025

Abstract. The inverse problem in quantitative photoacoustic imaging (QPAI), particularly in optical inversion, presents significant challenges for accurate image reconstruction due to the nonlinearity of photoacoustic signal. In this study, we introduce a novel reconstruction strategy specifically tailored for imaging the intervertebral disc (IVD), a biphasic tissue primarily composed of water and collagen. This work offers two key contributions: (1) the development of a new model-based optical inversion method that leverages the ratio of multi-wavelength photoacoustic measurements to define the cost function—circumventing the need for prior knowledge of the Grüneisen parameter, which is typically difficult to estimate; and (2) a first demonstration of QPAI's potential to non-invasively probe the biochemical composition of the IVD, particularly its water-to-collagen ratio. A non-linear model-based reconstruction approach was implemented, using the adjoint variables method to express gradients, and Monte Carlo simulations to solve the Radiative Transfer Equation for both the forward and adjoint problems. Several scenarios were investigated, and a method was proposed that does not rely on prior knowledge of the Grüneisen coefficient. A numerical study was conducted using a digitised pig's disc and opto-mechanical properties sourced from the literature, under measurement configurations compatible with experimental setups. The results show that the derived ratio-based cost function in the model-based optical inversion scheme significantly enhances the reconstructions quality, particularly when combined with appropriate regularisation, thereby validating the feasibility and robustness of the approach. Tridimensional reconstructions of the two chromophores content in the IVD, performed under the highly restricted configuration of a single illumination, were obtained with less than 5% error, along with the reconstruction of the Grüneisen coefficient with less than 15% error, up to 2 cm in depth (noiseless synthetic data) with the proposed method, with only three different wavelength measurements required.

1. Introduction

In this paper, we propose a method based on quantitative photoacoustic imaging (QPAI) to assess to both the molecular content and mechanical properties of a given organ. In this study, the intervertebral disc (IVD) is considered within a sensing configuration compatible with examination under surgery [1], though the method can be easily adapted for other organs with different molecular composition.

The purpose of QPAI is to provide an accurate estimation of the concentrations of chromophores through illumination at multiple wavelengths and known molecular extinction spectra of elementary chromophores. In the literature, QPAI has been used to estimate vital physiological parameters such as haemoglobin concentration [2, 3], oxygen saturation [4, 5], melanin, lipids or water constitution [6, 7, 8] in various organs [9]. Specifically designed exogenous contrast agents can also be used to provide additional molecular or functional information, to facilitate the visualisation and characterisation of specific biomarkers, and to aid the diagnosis and monitoring of diseases such as cancer [10].

However, one major problem in QPAI is, in most cases, the Grüneisen parameter, which self-consistently accounts for the mechanical properties of the probed medium, is typically assumed to be known. Different strategies have been proposed to circumvent this assumption, typically involving multiple illumination measurements at different locations [11, 12]. Here, an alternative approach is proposed, based on localised spectroscopic measurements, that we compared in the present study to the conventional approach consisting of assuming the Grüneisen coefficient known.

Our developments are driven by the medical motivation to create a simple, fast, and flexible method for quantifying the molecular composition of the intervertebral disc (IVD), in a sensing configuration compatible with surgery in the operating room. The IVD is a fibrocartilaginous structure, primarily composed of water and collagen, that ensures the cohesion and mobility of the spine. Furthermore, its unique collagen fiber arrangements, combined with a high level of hydration confer the IVD impressive mechanical properties that support heavy loads while preserving its integrity. Therefore, quantitatively accessing to both the molecular content and the Grüneisen parameter, is of paramount interest for practical diagnosis as well as fundamental biomechanical research of this organ.

In PA imaging, the full inverse problem involves recovering the optical parameters, or molecular content (when spectroscopic measurements are considered), from peripheral measurements of the photoacoustic (PA) waves. This complex problem can be addressed [13, 14, 15] by deriving the spatio-temporal expressions of gradients that account for the light fluence distribution and the propagation of acoustic waves through the tissues. The computational burden is alleviated by dividing the problem into two sequential inverse problems: first, the acoustic inverse problem to recover the initial pressure distribution in the tissue from the detected acoustic signal (e.g. model-based, filtered back-projection, time-reversal, delay-and-sum, deep learning [16]), and second, the

optical inverse problem to reconstruct the optical properties or molecular content of the tissue from this initial pressure distribution [17, 18]. The acoustic inverse problem has been extensively addressed in the literature, with exact solutions existing for cases involving complete data and acoustically homogeneous tissue [19]. Several methods have been specifically developed to handle the more challenging case of inhomogeneous acoustic properties [20, 21]. In this initial demonstration, we focus solely on the optical inverse problem, within the simplified scenario of an already reconstructed initial pressure distribution, p. This measurement, p, at position $\mathbf{r}$ in a medium illuminated by a pulsed source (e.g., laser) with wavelength λ, is expressed as:

$$p(\mathbf{r}, \lambda) = \Gamma(\mathbf{r})\mu_a(\mathbf{r}, \lambda)\Phi(\mu_a(\mathbf{r}, \lambda), \mu_s(\mathbf{r}, \lambda), g(\mathbf{r}, \lambda)), \tag{1}$$

with Γ the Grüneisen parameter (dimensionless), μ_a the absorption coefficient (m^{-1}), μ_s the scattering coefficient (m^{-1}), g the anisotropy coefficient (dimensionless) and Φ the fluence ($\mathrm{W.m}^{-2}$). The main objective of the optical inverse problem is to recover these coefficients. However, this task is not straightforward, as on the one hand, the fluence, and consequently the pressure rise p, is non-linearly related to μ_a, μ_s, and g, and, on the other hand, Γ, although often assumed to be homogeneous and known in many studies, is in fact also a spatially varying unknown that needs to be considered. Several challenges arise from this statement, the primary one being the non-uniqueness of the solution. The method introduced hereafter allows for the elimination of the contribution of the mechanical properties in the reconstruction of the optical parameters.

To remotely quantify the three-dimensional (3D) distribution of the elementary constituents of the IVD, several strategies can be employed. Linear methods have been found to be less accurate due to their dependence on the estimation of fluence, which is challenging to obtain, and non-linear methods are expected to yield more accurate results. For instance, Bal and Ren [22] proposed rearranging the light propagation model (Diffusion Approximation) using multiple wavelengths and illumination patterns to reconstruct absorption and scattering coefficients, as well as the Grüneisen parameter. The fixed-point iteration method [23] requires knowledge of the scattering coefficient, limiting its applicability and compromising the accuracy of any quantification, even with an approximate estimate of the scattering coefficient. The spatial frequency separation method [24] operates effectively when the absorption coefficient and fluence exhibit distinct frequencies, which is not typically the case within the IVD where chromophore distribution varies continuously throughout the organ. Deep learning methods [25, 26] require extensive biomedical datasets on IVD composition and degeneration states, which are currently not readily available. Therefore, these methods were not considered within the scope of this work.

In this study, the model-based inversion method has been selected to solve the optical inverse problem in QPAI. This approach is particularly flexible and can be easily adapted, particularly for incorporating prior information and regularisation. This method has been applied with various models of light propagation, such as the Diffusion

Approximation [27, 28, 29] or the more comprehensive Radiative Transfer Equation (RTE) [30, 31, 32], as chosen in this paper. Within this framework, there are different ways to minimise the cost function, ranging from methods with slower convergence rates but lower computational costs (e.g. gradient descent or quasi-Newton methods) to faster convergence methods that require higher computational and memory resources (e.g. Newton method, Gauss-Newton). Model-based inversion can also be combined with Bayesian methods [29, 33], which provide effective ways to integrate prior information and address measurement noise perturbations. However, these Bayesian methods involve the computation of large matrices (e.g., covariance), which can pose significant memory requirements, particularly in 3D scenarios. Given the complexity and the number of unknowns in the IVD, the gradient descent method was deemed more suitable and has been employed here to minimise the cost function efficiently.

In the present paper, a numerical study is conducted to explore the possibility of using QPAI as a method to quantify opto-mechanical parameters (collagen and water content, and Grüneisen parameter) of the IVD, essential information to assess *in fine* its pathological state. We explored various strategies to reconstruct the opto-mechanical parameters throughout the entire volume of the IVD, considering a single source illumination, compatible with surgical situation, and limited spectroscopic measurements. We considered three scenarios: (i) the Grüneisen coefficient is known, spatially homogeneous across the IVD, and set here to a value of 1; (ii) it is known and assumed to vary according to an arbitrary, yet specified, phenomenological law relating it to the chromophore concentrations; and (iii) it is entirely unknown. These scenarios ranged from unrealistic situations, though widely adopted in the literature, where the Grüneisen parameter is known and spatially invariant to more realistic scenarios where no prior knowledge is assumed. While the first scenario is a simplification that deviates significantly from reality, as it is commonly used, it serves as the reference method in this study. The second scenario highlights the potential to recover the unknown parameters, provided that advancements are made in the experimental characterisation of the IVD, particularly regarding its chromophore composition. The third is our novel method that does not rely on any prior information about the mechanical properties of the IVD. In the latter case, the advantage of using spectroscopic measurements with multiple degrees of freedom is fully leveraged. Since the Grüneisen parameter conveys purely mechanical information, it remains independent of wavelength. A reference measurement is chosen as a baseline, typically acquired at one pre-selected wavelength, and subsequent measurements are normalised relative to this baseline. A flowchart describing the essential steps of the model-based optimisation process can be found in Fig. 1. The inverse problem is formulated in section 2. A model-based gradient descent inversion scheme was implemented, using the RTE as the light propagation model. Gradients were derived with the adjoint method: forward and adjoint RTE problems were solved with Monte Carlo (MC) simulations. The spherical harmonics expansion was introduced to handle the angular distribution of the photometric quantities as an efficient and accurate way to reduce the calculation workload [34, 35] and was already

adapted and shown to be feasible for the IVD exploration and the reconstruction of the absorption coefficient from a single wavelength illumination [32]. Section 3 provides a detailed analysis of the morphology of the IVD and a comprehensive literature review of its opto-mechanical properties to design a realistic digital twin described in section 4. This section provides a detailed explanation of the methodology used to generate synthetic PA measurements. The results are then reported in section 5 and further discussed in section 6, and finally we conclude in section 7. The results demonstrated the feasibility of the QPAI for the 3D reconstruction of the entire set of opto-mechanical properties of the IVD, without strong prior knowledge.

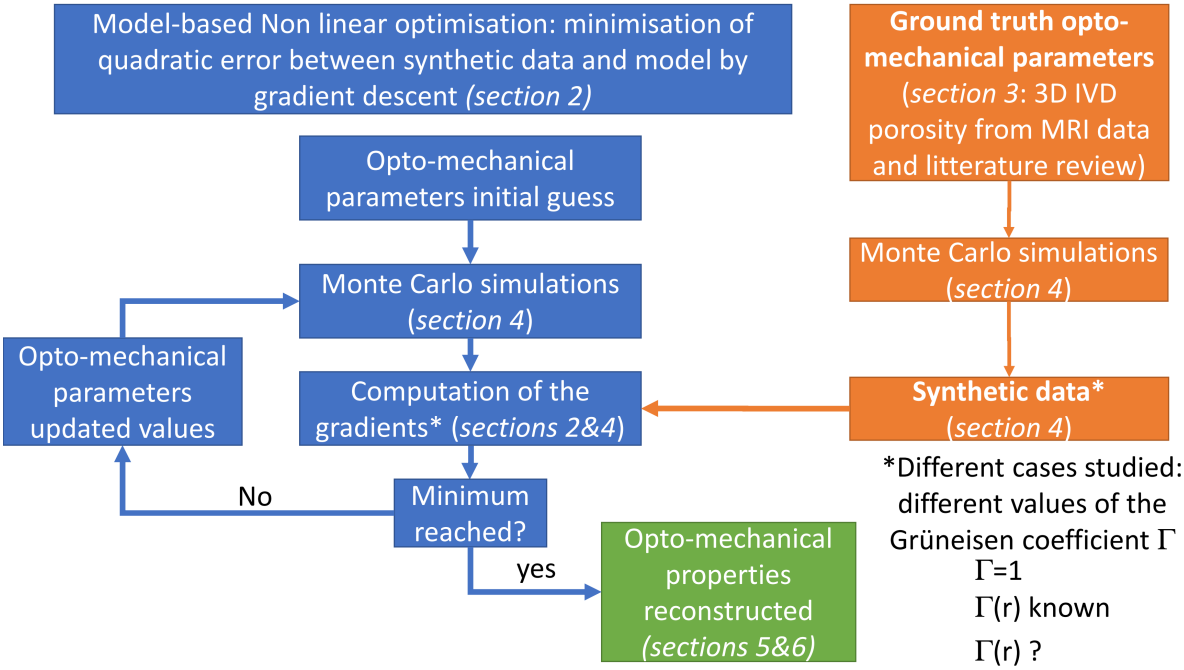

Figure 1. Flowchart describing the different steps of the model-based optimisation process.

2. Inverse problem formulation

In this section, the inverse problem is formulated non-linearly by minimizing a cost function, initially assuming a known Grüneisen parameter, as is commonly done in the literature. Subsequently, a method is proposed that avoids this restrictive assumption. From the measurements p^e, the objective is to recover the unknowns of interest x (absorption μ_a, scattering μ_s coefficients, Grüneisen parameter Γ, chromophores' proportions r_c, r_w) using a model-based inversion. This is achieved through the minimisation with gradient descent of the following cost function :

$$\epsilon = \frac{1}{2}\|p^e - p_0(x)\|_2^2 = \frac{1}{2}\int_\Omega (p^e - p_0(x))^2 d\mathbf{r} = \sum_{i\in[1,N]} \frac{1}{2}\int_\Omega \left(p^e(\lambda_i) - p_0(\lambda_i)\right)^2 d\mathbf{r}, \qquad (2)$$

Ω representing the IVD volume, and $p_0 = \Gamma\mu_a\Phi$, and N the number of wavelengths considered. Hence, the expressions of the gradients with respect to the chromophores' proportions depend on the optical parameters (μ_a, μ_s) but also on the Grüneisen parameter. In the situation where a relationship between Γ and the chromophore composition can be established (Eq.12), these expressions can be derived. Alternatively, since the Grüneisen parameter is wavelength-invariant, we propose here to normalise the spectroscopic measurements to a chosen reference wavelength:

$$\epsilon = \sum_{\substack{i,j\in[1,N]\\ i\neq j}} \frac{1}{2}\int_\Omega \left(\frac{p^e(\lambda_i)}{p^e(\lambda_j)+\tau} - \frac{p_0(\lambda_i)}{p_0(\lambda_j)+\tau}\right)^2 d\mathbf{r}. \tag{3}$$

As a result, this method does not require any information on the Grüneisen parameter. A weak regularisation parameter τ was introduced in the denominators to prevent instability, which can occur particularly in deeper areas where computed fluence values are low and noise has a greater influence. Its effect is studied and discussed (see section 6.3). There are more conventional methods to regularise the problem, such as adding a penalty term to the cost function to favor certain types of solutions. For example, we can mention L1 and L2 regularisation, which are the most common ones, but more complex forms of regularization also exist.

2.1. Expression of the cost function gradients with known expression of Γ

In order to perform the gradient descent, the derivatives of the cost function ϵ (Eq. 2) with respect to the parameters of interest need to be calculated. In the present case, the parameters of interest are the proportions of concentrations of collagen r_c and water r_w, and the Grüneisen parameter Γ. Let's first look at the differential $d\epsilon$:

$$d\epsilon = \int_\Omega (p^e - p_0)(-dp_0)d\mathbf{r} = -\int_\Omega (p^e - \Gamma\mu_a\Phi)(d\Gamma\mu_a\Phi + \Gamma d\mu_a\Phi + \Gamma\mu_a d\Phi)d\mathbf{r}. \tag{4}$$

In the framework of this paper, the RTE is considered to be the light propagation model, and the expressions of the gradients are derived through the introduction of the Adjoint RTE (ARTE)[30, 36]. Both equations can be written as:

$$(\mathcal{S}\cdot\nabla + \mu_a(\mathbf{r}) + \mu_s(\mathbf{r}))\mathcal{L}(\mathbf{r},\mathbf{s}) = \mu_s(\mathbf{r})\int_{4\pi}\Theta(\mathbf{s},\mathbf{s'})\mathcal{L}(\mathbf{r},\mathbf{s'})d\mathbf{s'} + \mathcal{Q}(\mathbf{r},\mathbf{s}), \tag{5}$$

with $\mathcal{L} \equiv \{L, L^*\}$, $\mathcal{Q} \equiv \{q, q^*\}$ and $\mathcal{S} \equiv \{\mathbf{s}, \text{-}\mathbf{s}\}$, where L is the radiance, and q the source term in the RTE, and L^* the adjoint radiance, and q^* the adjoint source term in the ARTE, equal to $q^* = \Gamma\mu_a\Delta p$ where $\Delta p = (p^e - \mu_a\Phi)$. Θ is the phase function. The Henyey-Greenstein function was used to describe its behavior. Hence, $d\epsilon$ is now linearly expressed in terms of the derivatives of the ones of the physical parameters:

$$\begin{aligned} d\epsilon = &-\int_\Omega d\Gamma d\mathbf{r}\,(\Delta p\mu_a\Phi) - \int_\Omega d\mu_a d\mathbf{r}\left(\Delta p\Gamma\Phi - \int_{4\pi} L(\mathbf{s})L(\mathbf{s})^* d\mathbf{s}\right) \\ &+ \int_\Omega d\mu_s d\mathbf{r}\int_{4\pi}\left(L(\mathbf{s})L(\mathbf{s})^* - \int_{4\pi} L^*(\mathbf{s'})\Theta(\mathbf{s},\mathbf{s'})L(\mathbf{s'})d\mathbf{s'}\right)d\mathbf{s}. \end{aligned} \tag{6}$$

The gradient ∇_x over any parameter of interest x, at any position $\mathbf{r} = r_0$ can now be easily expressed:

$$\begin{aligned}
\nabla_{\mu_a}|_{\mathbf{r}=\mathbf{r}_0} &= -\Delta p(\mathbf{r}_0)\Gamma(\mathbf{r}_0)\Phi(\mathbf{r}_0) + \int_{4\pi} L(\mathbf{r}_0,\mathbf{s})L^*(\mathbf{r}_0,\mathbf{s})d\mathbf{s}, \\
\nabla_{\mu_s}|_{\mathbf{r}=\mathbf{r}_0} &= \int_{4\pi}\left(L^*(\mathbf{r}_0,\mathbf{s})L(\mathbf{r}_0,\mathbf{s}) - \int_{4\pi} L^*(\mathbf{r}_0,\mathbf{s'})\Theta(\mathbf{r}_0,\mathbf{s},\mathbf{s'})L(\mathbf{r}_0,\mathbf{s})d\mathbf{s'}\right)d\mathbf{s}, \\
\nabla_{\Gamma}|_{\mathbf{r}=\mathbf{r}_0} &= -\Delta p(\mathbf{r}_0)\mu_a(\mathbf{r}_0)\Phi(\mathbf{r}_0),
\end{aligned} \tag{7}$$

By considering their linear relationship, through a mixing law, between the absorption and scattering coefficients and the chromophore content :

$$\mu_a(\mathbf{r},\lambda) = \alpha_c(\lambda)r_c(\mathbf{r}) + \alpha_w(\lambda)r_w(\mathbf{r}) \text{ and } \mu_s(\mathbf{r},\lambda) = \sigma_c(\lambda)r_c(\mathbf{r}) + \sigma_w(\lambda)r_w(\mathbf{r}), \tag{8}$$

where $r_c(\mathbf{r})$ and $r_w(\mathbf{r})$ are the proportions of collagen and water at position $\mathbf{r}$, respectively (r_c and r_w are between 0 and 1), and α_c and α_w are the specific absorption of collagen and water, respectively,σ_c is the scattering coefficient of collagen, water being non scattering $\sigma_w = 0$. The gradients with respect to the collagen and water proportions can be derived straightforwardly:

$$\begin{aligned}
\nabla_{r_{c,w}}|_{\mathbf{r}=\mathbf{r}_0} =& \frac{\partial\mu_a}{\partial r_{c,w}}\frac{\partial\epsilon}{\partial\mu_a}|_{\mathbf{r}=\mathbf{r}_0} + \frac{\partial\mu_s}{\partial r_{c,w}}\frac{\partial\epsilon}{\partial\mu_s}|_{\mathbf{r}=\mathbf{r}_0} + \frac{\partial\Gamma}{\partial r_{c,w}}\frac{\partial\epsilon}{\partial\Gamma}|_{\mathbf{r}=\mathbf{r}_0} \\
=& \alpha_{c,w}(\mathbf{r}_0)\left[-\Delta p(\mathbf{r}_0)\Gamma(\mathbf{r}_0)\Phi(\mathbf{r}_0) + \int_{4\pi} L(\mathbf{r}_0,\mathbf{s})L^*(\mathbf{r}_0,\mathbf{s})d\mathbf{s}\right] \\
&+\sigma_{c,w}(\mathbf{r}_0)\left[-\int_{4\pi}\int_{4\pi} L^*(\mathbf{r}_0,\mathbf{s'})\Theta(\mathbf{r}_0,\mathbf{s},\mathbf{s'})L(\mathbf{r}_0,\mathbf{s})d\mathbf{s}d\mathbf{s'} + \int_{4\pi} L^*(\mathbf{r}_0,\mathbf{s})L(\mathbf{r}_0,\mathbf{s})d\mathbf{s}\right] \\
&-\mu_a(\mathbf{r}_0)\Delta p(\mathbf{r}_0)\frac{\partial\Gamma}{\partial r_{c,w}}|_{\mathbf{r}=\mathbf{r}_0}\Phi(\mathbf{r}_0).
\end{aligned} \tag{9}$$

Note that the expressions are written in our case for only two components; however the derivations can be generalised to any number of chromophores, provided their specific absorption spectra are known.

2.2. Expression of the cost function's gradients with an unknown expression of Γ *and normalised measurements*

To simplify the gradient calculation, consider two wavelengths λ_1 and λ_2 to define the cost function. The generalisation to multiple wavelength measurements is straightforward. The gradients with respect to the proportions $r_{c,w}$ are expressed as:

$$\begin{aligned}
\nabla_{r_{c,w}|_{\mathbf{r}=\mathbf{r}_0}} &= \int_\Omega \left(\frac{p^e(\lambda_1)}{p^e(\lambda_2)+\tau} - \frac{p_0(\lambda_1)}{p_0(\lambda_2)+\tau}\right)\left(-\frac{\partial}{\partial r_{c,w}}\frac{p_0(\lambda_1)}{p_0(\lambda_2)}\right)d\mathbf{r} \\
&\approx \int_\Omega \left(\frac{p^e(\lambda_1)}{p^e(\lambda_2)+\tau} - \frac{p_0(\lambda_1)}{p_0(\lambda_2)+\tau}\right)\left(-\frac{\mu_a(\lambda_1)\Phi(\lambda_1)}{\mu_a(\lambda_2)\Phi(\lambda_2)}\left(\frac{\alpha_{c,w}(\lambda_1)}{\mu_a(\lambda_1)} - \frac{\alpha_{c,w}(\lambda_2)}{\mu_a(\lambda_2)}\right)\right)d\mathbf{r},
\end{aligned} \tag{10}$$

assuming $\alpha_{c,w}(\lambda_i)\Phi_i >> \mu_a(\lambda_i)\frac{\partial\Phi_i}{\partial r_{c,w}}$, as the adjoint term is generally negligle [35] (a factor of more than 10^4 in amplitude was typically found between the two terms, results not shown). Note that using N wavelengths leads to N-1 ratios of measurements.

Once the proportions of chromophores are reconstructed, the Grüneisen parameter Γ can be calculated straightforwardly using any measurement, or multiple measurements, and the computation of the resulting absorption coefficient and fluence at the corresponding wavelengths according to the following expression:

$$\Gamma = \frac{1}{N}\sum_{i\in[1,N]}\frac{p^e(\lambda_i)}{\mu_a(r_c,r_w,\lambda_i)\Phi(r_c,r_w,\lambda_i)}. \tag{11}$$

3. Opto-mechanical properties of the intevertebral disc

This section provides morphological and functional details of the IVD. Its molecular composition along with a thorough literature review, enables the expression of the optical and mechanical parameters of the IVD, which are essential for modeling PA wave propagation.

3.1. Morpho-functional description of the organ

Located between adjacent vertebrae, the intervertebral disc (IVD) is an essential component of the spine, serving as a shock absorber and enabling flexibility and movement. It consists of a gel-like centre called the nucleus pulposus (NP) surrounded by a fibrous ring called the annulus fibrosus (AF) (Fig.2). The IVD distributes pressure evenly across the spine and maintains the spacing between the vertebrae. Over time, due to aging and wear and tear, the IVD can degenerate, leading to degenerative disc diseases (e.g. herniated discs, spinal stenosis), causing pain, stiffness, and nerve damage. This degeneration primarily arises from modification in its intrinsic composition. The IVD is essentially composed of water, collagen and proteoglycans [37], with their proportions varying depending on the region of the IVD, and also on its degeneration state.

The IVD contains a significant amount of water, which gives it a gel-like structure, particularly pronounced in the NP [38]. This water content decreases with age, contributing to degenerative disc diseases such as low back pain [39]. In the healthy NP, water constitutes approximately 80-90% of the chromophore content, whereas in the AF, it reduces to 65-70% [37] (Fig. 2). Collagen, the most abundant protein in the human body, is a fibrous protein that provides structural support and strength to various tissues, including skin, tendons, cartilage, bone, and blood vessels. In the IVD, collagen of types I and II constitutes 80% of the total collagen present in the disc [40]. Collagen is organised in complex lamellar weaves in the outer AF, accounting for 50-70% of its dry weight. In contrast, collagen makes up 10-20% of the dry weight in the NP, where it is sparsely distributed and randomly oriented[41]. Proteoglycans are complex macromolecules found in various tissues throughout the body, including cartilage, bone, skin, and blood vessels. In the IVD, proteoglycans play the crucial role of retaining the

water content. They represent 35-65% of the dry-weight in the NP *vs* 20% in the AF [38]. The amount of proteoglycans decreases with age, which is directly linked to the decrease in water content within the IVD. These values exhibit individual variations and are closely related to the degenerative state of the disc, highlighting the need for methods to accurately quantify this composition. These components, particularly water and collagen, exhibit specific optical signatures in the visible to near infrared spectrum (Fig. 2), quantified in terms of absorption and scattering coefficients spectra. Therefore, we propose to explore the possibility of using QPAI as a method to assess the state of viability of the IVD, as an alternative to Magnetic Resonance Imaging (MRI), which is the conventional and reference technique for high-resolution and quantitative imaging. In previous works [42], we have demonstrated the sensitivity of the PA signal to these chromophores with spectroscopic measurements.

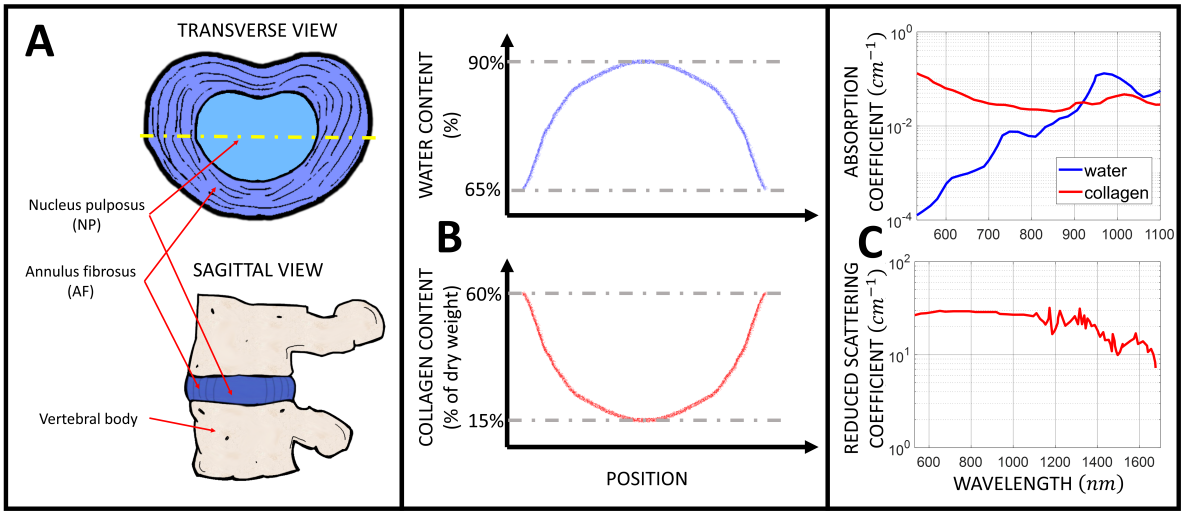

Figure 2. A) Illustration of the IVD and B) spatial variation of the water and collagen content in the disc along the yellow line in A. The variations in proteoglycan content are not shown as they exhibit a similar trend to water content. C) Absorption coefficients collagen and water (top) and reduced scattering coefficient of collagen (bottom). The values for collagen were obtained from measurements were extracted from [43], performed on flakes of type I collagen obtained from a bovine achilles tendon, and values for water from https://omlc.org/spectra/water/data/hale73.txt [44] .

3.2. Optical properties

The absorption and scattering coefficients were calculated using the proportion of chromophores at position **r** inside the disc. Limited information was found in the literature concerning the optical properties of proteoglycans. In all that follows, the absorption of the IVD was assumed to be exclusively due to water and collagen alone. However, all the methodologies and findings can readily be extended to incorporate other types of chromophores if their optical properties are known. In the case of the simulated biphasic IVD, these coefficients depend on the wavelength λ and can be written using

the mixing law 8. The absorption and reduced scattering coefficients spectra of these two chromophores are presented in Fig. 2 and are taken from [43]. The anisotropy factor g is, in general, difficult to measure, especially *in vivo* on tissues. As we couldn't find any elements in the litterature, this parameter was assumed to be equal to 0.9 in the IVD, a typical value found in most of biological tissues [45], and the scattering coefficient was therefore $\mu_s = \frac{\mu'_s}{1-g} = 10\mu'_s$.

3.3. Grüneisen parameter

Although the Grüneisen parameter is often assumed to be constant in the literature, this assumption is not realistic in the IVD. The distinct textures between the gelatinous and highly aqueous NP and the more rigid AF ensure spatial heterogeneity in mechanical properties throughout the disc. Therefore, the Grüneisen parameter was defined here as chromophore-dependent, spatially-varying and calculated using the thermo-mechanical properties of water and collagen according to the following equation: $\Gamma = (\beta v^2)/C_p$, with β the volumetric thermal expansion coefficient ($^\circ\mathrm{C}^{-1}$), v the speed of sound ($\mathrm{m.s}^{-1}$) and C_p the specific heat ($\mathrm{J.kg}^{-1}.^\circ\mathrm{C}^{-1}$). Values for β, v, and C_p of collagen and water were obtained from the literature, and are presented in table 1. Unfortunately, the speed of sound for collagen was not found, but an empirical expression was obtained from [46] that relates the velocity of sound to the percentage of collagen present in a tissue: $v(r_c) = 1588 + 32ln(100r_c)$. This relation was derived by gathering speed of sound of tissue with different collagen concentrations in the literature and fitting an expression to these values. In the absence of other references, this expression was used here to model the speed of sound within the IVD. The other parameters were defined by considering the proportion of water and collagen at position $\mathbf{r}$ in the IVD using a mixing law. The resulting expression for the Grüneisen parameter is therefore:

$$\Gamma = \frac{(\beta_w r_w + \beta_c r_c)(1588 + 32ln(100r_c))^2}{C_{p,w} r_w + C_{p,c} r_c} \tag{12}$$

Table 1 compares the values derived using the mixing law with those of typical cartilage, except for the thermal expansion coefficient, which lacks a corresponding value for cartilage. The specific heat capacity, C_p, is consistent the documented range in the literature. The speed of sound, v, shows a slightly higher value, but remains within a close range.

4. Synthetic data generation on a digital phantom and gradients computation

A series of measurements were performed *in silico*. This section provides a description of the digital phantom and the numerical details for computing the gradients. All computations were run on a desktop equipped with processor Inter Xeon E5-1620, 8 cores, 3.50GHz, with Graphics Processor Unit Quadro P6000.

	Water	Collagen	20% collagen 80% water	Cartilage range values
β (K^{-1})	206×10^{-6} [47]	540×10^{-6} [48]	272×10^{-6}	
v $(m.s^{-1})$	1483 [49]	/	1683	1627-1650 [50]
C_p $(J.K^{-1}.kg^{-1})$	4180 [51]	1300 [52]	3604	3500-3664 [50]

Table 1. Volumetric thermal expansion β, speed of sound v and specific heat C_p of collagen and water at 20°C. The values obtained from a mixing law (20% collagen and 80% water) and the values range for cartilage found in the literature are presented as well for comparison.

4.1. Digital phantom and opto-mechanical properties

The morphology of the IVD and the corresponding porosity map were obtained from proton density-weighted MRI scans of the IVD of a 4-month-old pig, as reported in [53] and are presented in Fig.3, first row.

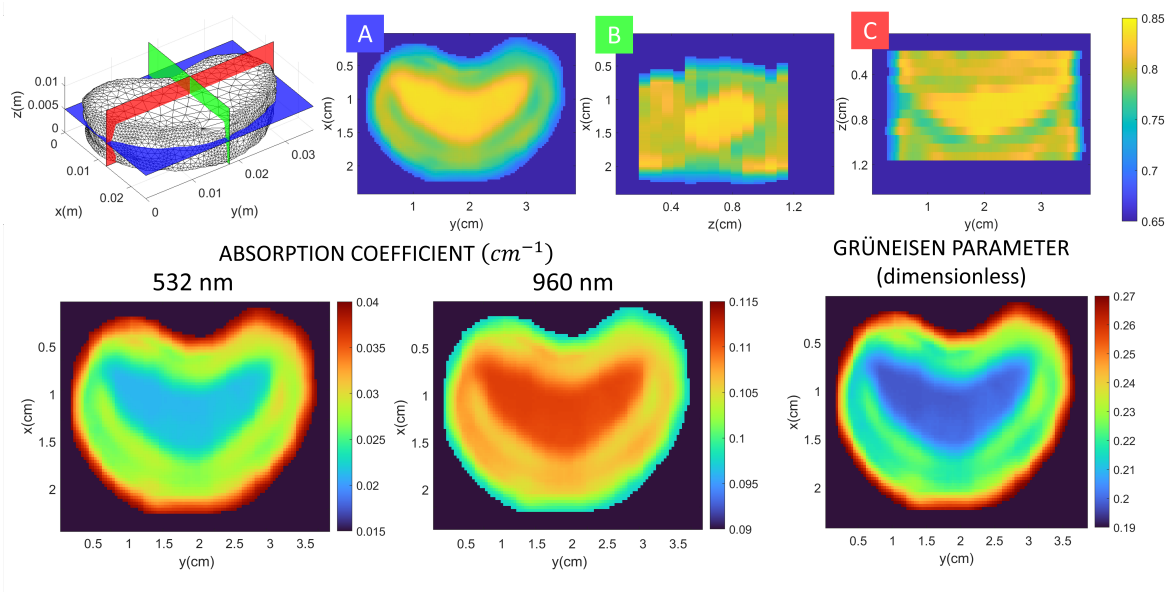

Figure 3. 3D morphology of the IVD and porosity map (dimensionless) in the three centred 2D planes (A, B, C, top). Absorption coefficient (in cm^{-1}) related to the porosity map at 2 different wavelengths (532 nm and 960 nm) and Grüneisen parameter Γ (dimensionless) in the intervertebral disc related to the porosity map and (12) (bottom).

The imaged disc is approximately 0.8 cm×2.5 cm×3.5 cm. This 3D digitised morphology was projected into a 77×104×19 voxel grid. In this grid, the IVD is represented by approximately 65,000 independent voxels. From these MRI data, one can extract the porosity, which corresponds to the proportion of void space over the total volume in an object. In the case of saturated media, such as the IVD, the porosity is equivalently expressed as the proportion of water over the total volume [53], from which the spatial distribution of the water proportion r_w inside the disc can be determined. This proportion of water r_w varies from 85% inside the NP and smoothly decreases as

one moves radially reaching 70% at the outer borders of the AF. This behaviour is in agreement with values found in the literature and presented in section 3. With the proteoglycan content neglected, the IVD is considered here as a biphasic medium. The collagen proportion r_c is assumed to be the remaining component in the disc, following the relation $r_c = 1 - r_w$. Although synthetic, realistic maps of the opto-mechanical properties of the IVD can be generated (Fig.3, second row).

4.2. Generation of synthetic measurements

We consider the experimental setup described in [42]: the source (diameter 1 cm) irradiates one side of the IVD (Fig. 4) with multiple wavelengths, targeting the thickest region of the disc ($\sim$ 3 cm). It is worth noting that this represents the most unfavorable case when probing the disc, as in practice during surgery, it is probed from a ventral side (illumination from the bottom in the schema Fig. 4, Left), where the IVD's thickness is typically smaller ($\sim$ 1.5 cm). Note that the IVD is supposed to be immersed in water for acoustic impedance matching, which is an over-simplified situation that we consider to be sufficient to demonstrate the efficacy of the proposed approach. Further developments need to be include an acoustic propagation model that accounts for strong impedance mismatch occurring at the vertebral boundaries. The fluence Φ and the initial pressure distribution $p(\mathbf{r})$ were then computed with MC simulations with the versatile open-source codebase MCmatlab software [54] which inputs are the spatial distribution of the optical parameters $\mu_a(\mathbf{r})$, $\mu_s(\mathbf{r})$ and g, for the considered wavelength λ, and the source term. This one is supposed to be a continuous wave (CW, under usual assumptions of stress and thermal confinement with short pulsed illumination [55]) top-hat extended source (diametre 1 cm, Fig. 4) illuminating the disc under normal incidence. MCmatlab allows the storage of the power (or photon weight) $dW_k(\mathbf{r})$ deposited by the k^{th} photon at the position $\mathbf{r}$. The total normalized power per voxel is obtained in output as $W(\mathbf{r}) = \frac{1}{N_{ph}} \sum_{k=1}^{N_{ph}} dW_k(\mathbf{r})$, with $N_{ph} \sim 10^8$, in a 77×104×19 voxels volume, from which one can obtain : i) the fluence as $\Phi(\mathbf{r}) = W(\mathbf{r})/\mu_a(\mathbf{r})$ and ii) the initial pressure distribution as $p(\mathbf{r}) = \Gamma(\mathbf{r}) \times W(\mathbf{r}))$ maps (Fig. 3). An example of a initial pressure distribution measurement obtained at 532 nm is presented in Fig. 4.

Let's consider N measurements $\hat{p}_n \in \mathcal{R}^P$, $n \in [1, N]$ obtained at N wavelengths. $\hat{p}$ is a vector containing the N measurements: $\hat{p} = (\hat{p}_1, ..., \hat{p}_N) \in \mathcal{R}^{PN}$. As previously mentioned, the measurements are obtained numerically and are discretised in a 3D grid containing P =77×104×19 voxels. The reconstructions are performed on a grid with a different dimension to avoid the "inverse crime" [56]. A simple linear interpolation was sufficient since the variations in the measurements are sufficiently regular and smooth. This reconstruction grid is composed of Q =39×52×10 voxels. The measurements are resized by linear interpolation in the coarser grid dimension. The resized measurements are designed as $p = (p_1, ..., p_N) \in \mathcal{R}^{QN}$. Noise $e \in R^{QN}$ was added to the measurements as an additive value: $p^e = p + e$, e represents the noise vector which contains the noise in the N different measurements $e = (e_1, ..., e_N)$. The noise is supposed here to follow

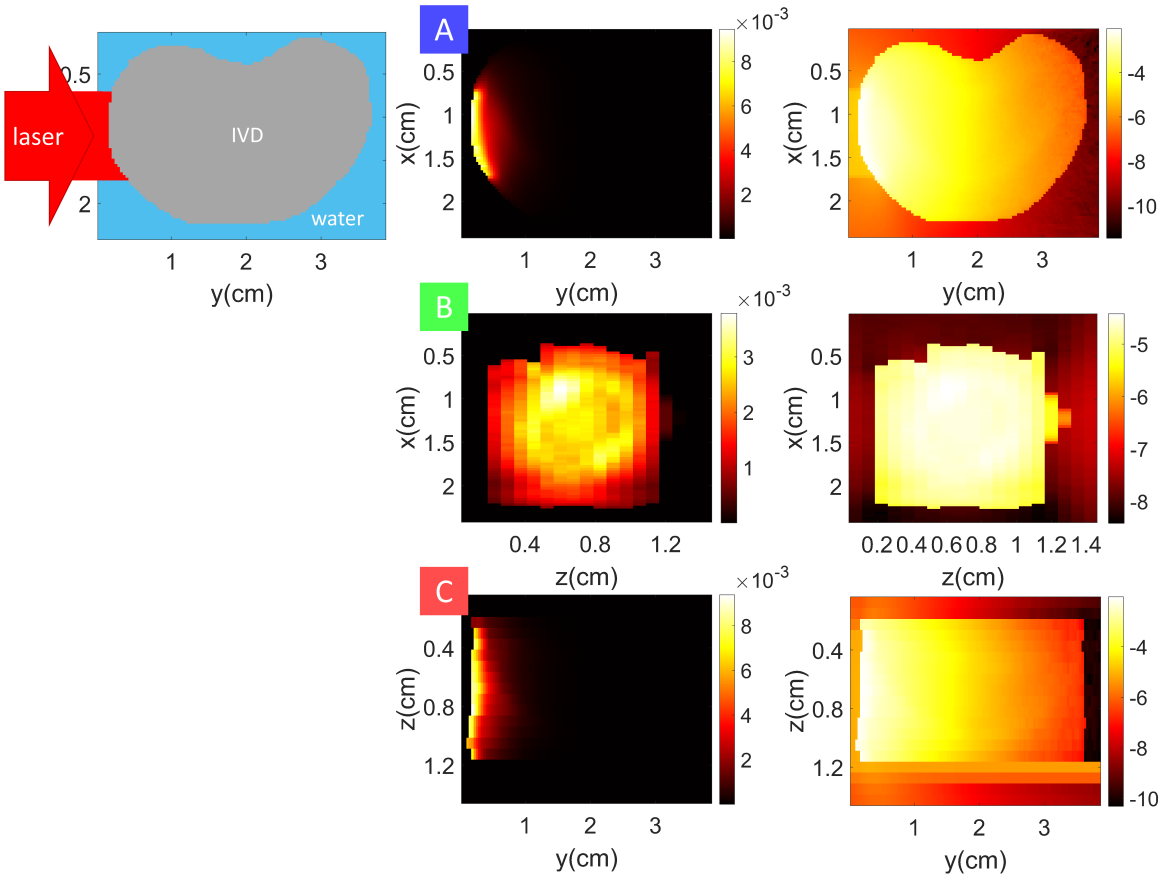

Figure 4. Left: schema of source configuration. Middle, example of a synthetic PA measurement $p = \Gamma \mu_a \Phi$ obtained at 532 nm in different centred planes of the IVD (A: yz-plane, B: xz-plane and C: xy-plane). Right: measurements in log scale.

a normal distribution with mean value $M_e = (M_{e,1}, ..., M_{e,N}) \in \mathcal{R}^{QN}$ and covariance $V_e = diag(V_{e,1}, ..., V_{e,N}) \in \mathcal{R}^{QN \times QN}$. In the case of white gaussian noise, which is the supposed case for all the following reconstructions, the mean M_e is equal to 0. For $n \in [1, N]$, the variance $V_{e,n}$ is defined as:

$$V_{e,n} = \left(\frac{k_{noise}}{3} \left(max(p_n) - min(p_n) \right) \right)^2 I_{Q \times Q}, \tag{13}$$

with $I_{Q \times Q}$, the identity matrix $\in \mathcal{R}^{Q \times Q}$ and k_{noise}, a parameter tuning the intensity of the noise.

Considering the IVD as a biphasic medium, two measurements performed at two different wavelengths are theoretically sufficient for an accurate reconstruction of the two proportions. Therefore, we limited ourselves to using this minimum of required measurements. The spectra of water and collagen (Fig.2) show that the two wavelengths 532 nm and 960 nm are of particular interest since they correspond to the minimum and maximum absorption ratios of water to collagen, respectively, and are chosen in this study. More complex spectra or additional chromophores, optimisation of the number

of spectral bands can be performed using the method outlined in [57].

4.3. Computation of the gradients

4.3.1. Spherical Harmonics expansion The calculation of the gradients Eqs. (7-10) requires the forward L and adjoint L^* radiances to be computed, both depending on the position $\mathbf{r}$ and the direction $\mathbf{s}$. Storing them at each ($\mathbf{r}$,$\mathbf{s}$), e.g. by discretising the unit sphere into segments for each position, is computationally demanding (Discrete Ordinates Method). Instead, the Spherical Harmonics (SH) expansion to store the directional information [58, 34, 35] was adopted: the radiances L, L^* and phase function Θ are decomposed into sums of Y_{lm} SH of order m and degree l:

$$\begin{aligned} L(\mathbf{r},\mathbf{s}) &= \sum_{l=0}^{N_{SH}} \sum_{m=-l}^{l} i_{lm}(\mathbf{r}) Y_{lm}(\mathbf{s}); L^*(\mathbf{r},\mathbf{s}) = \sum_{l=0}^{N_{SH}} \sum_{m=-l}^{l} i^*_{lm}(\mathbf{r}) Y^*_{lm}(\mathbf{s}); \\ \Theta(\mathbf{s},\mathbf{s'}) &= \sum_{l=0}^{N_{SH}} \sum_{m=-l}^{l} g^l Y^*_{lm}(\mathbf{s'}) Y_{lm}(\mathbf{s}), \end{aligned} \tag{14}$$

with N_{SH} the selected order of sum truncation. The Y_{lm} are calculated using the associated Legendre polynomials of degree l and order m. Using the Henyey-Greenstein phase function and the properties of orthonormality of the SH lead to simplified expressions of the gradients:

$$\nabla_{\mu_a}|_{\mathbf{r}=\mathbf{r}_0} = -\Delta p \Gamma \Phi + \sum_{l=1}^{N_{SH}} \sum_{m=-l}^{l} (i_{lm} i^*_{lm}); \nabla_{\mu_s}|_{\mathbf{r}=\mathbf{r}_0} = \sum_{l=1}^{N_{SH}} \sum_{m=-l}^{l} (1-g^l)(i_{lm} i^*_{lm}). \tag{15}$$

MCmatlab [54] was slightly modified to allow storage of the directional information of the travelling photons by projecting the photon energy into the corresponding SH [59, 34]:

$$i_{lm}(\mathbf{r}) = \frac{1}{N_{ph}} \sum_{k=1}^{N_{ph}} dW_k(\mathbf{r}) Y_{lm}(\mathbf{s}), \tag{16}$$

with $\mathbf{s}$ the incoming direction of the photon entering the voxel. Typical values of $N_{ph} \sim 10^6$ photons are sufficient in the present cases to accurately sample the radiances L. The same approach was adopted to compute the adjoint radiance L^* by modifying the source term. One major difference (and difficulty) between adjoint and forward models is that the adjoint source is generally internally distributed in the medium as $q^* = \Gamma \mu_a (p^e - \mu_a \Phi)$. Furthermore, because this source is defined as the difference between the measurement p^e and the model $p_0 = \mu_a \Phi$, photons launched from the adjoint source can have negative values. The MC algorithm treats negative weight photons the same way as positive ones by progressively reducing their weight (absolute value) to zero, allowing negative (reduction of) energy deposition into the voxels.

However, as in [35], we found that the contribution of derivative $d\Phi$ in the gradients that need the computation of the adjoint radiance can be neglected, significantly improving computation time.

4.3.2. Gradient descent Due to the stochastic nature of MC simulations, the computed gradients are subject to noise. Additionally, these gradients are large due to the 3D nature of the problem being addressed. To resolve these issues, the ADAM algorithm [60] was chosen to compute the step size in the gradient descent optimisation process. At each step iteration i, the mean m_i and the uncentered variance v_i of the gradient are calculated, with $g_i = \frac{\partial \epsilon}{\partial x}$,the stored gradient over the parameter of interest x: $m_i = \beta_1 m_{i-1} + (1-\beta_1) g_i$; $v_i = \beta_2 v_{i-1} + (1-\beta_2) g_i^2$. The hyperparameters β_1 and $\beta_2 \in [0, 1]$ control the exponential decay of the computed moving averages. They were set at the recommended values from [60]: $\beta_1 = 0.9$, $\beta_2 = 0.999$. At the initial step the moving averages v_0 and m_0 are initialised to 0, which biases the moments estimation towards zeros. Bias-corrected first and second raw moments are estimated: $\hat{m}_i = \frac{m_i}{1-\beta_1^i}$; $\hat{v}_i = \frac{v_i}{1-\beta_2^i}$. The parameters are then updated as:

$$x^{i+1} = x^i - t \frac{\hat{m}_i}{\hat{v}_i + e_{ADAM}} \tag{17}$$

with t the learning rate and e_{ADAM} a small value to avoid division by zero. Here also, as recommended [60], these parameters are set at $e_{ADAM} = 10^{-12}$ and $t = 0.001$. In order to limit the computation time while keeping sufficient accuracy, all MC simulations involved in the computation of the gradients were limited to 10^6 photons. This represents the heaviest burden in the computation of the gradients, with a computation time of ~ 1 min per iteration for Eqs. 9 and 10, if the adjoint term is neglected. The algorithms are stopped when the variation of the cost function $\Delta\epsilon$ goes below a certain threshold, which is bound to vary depending on the reconstructed parameter (μ_a, μ_s, $r_{c,w}$, and/or Γ) and the number of measurements used. The stopping criterion is set at $\Delta\epsilon = 10^{-8}$ for all reconstructions, except for those employing the measurement ratio method. Due to potential instability in this method, which varies with the value of τ, reconstructions using the measurement ratio method were terminated after 400 iterations. Any deviations from these specified criteria will be explicitly stated.

4.3.3. Metrics for quantifying the reconstructions quality In order to quantify the efficiency of the performed reconstructions, the reconstructions are represented along with error maps between the reconstructed parameters and the ground truth values, defined as $|(\hat{x}(\mathbf{r}) - x(\mathbf{r}))/x(\mathbf{r}| \times 100$, and the following global comparison metrics are used: Mean Squared Error (MSE), Peak Signal-to-Noise Ratio (PSNR) and Structural Similarity Index Measure (SSIM):

$$MSE = \frac{1}{n^2} \sum_{\mathbf{r}=1}^{n} [\hat{x}(\mathbf{r}) - x(\mathbf{r})]^2; PSNR = 20 \log_{10} \frac{I_{max}}{\sqrt{MSE}}; SSIM = \frac{(2\mu_x \mu_{\hat{x}} + C1)(2\sigma_{x,\hat{x}} + C2)}{(\mu_x^2 + \mu_{\hat{x}}^2 + C1)(\sigma_x^2 + \sigma_{\hat{x}}^2 + C2)}, \tag{18}$$

with n the number of data, $\hat{x}$ the reconstructed variables and x the ground truth; μ_x and $\mu_{\hat{x}}$ their mean values, σ_x and $\sigma_{\hat{x}}$ their variances, and $\sigma_{x,\hat{x}}$ the covariance matrix between those two variables. I_{max} corresponds to the maximum signal value in our original ground truth image. C1 and C2 are two values expressed as $C1 = (k_1 a)^2$ and $C2 = (k_2 a)^2$ with a the dynamic range of the voxel values. k_1 and k_2 are small constants, generally, chosen values are $k_1 = 0.01$ and $k_2 = 0.03$ based on the arbitrary choice of [61]. They found that in their experiments, the performance of the SSIM was unchanged to variations of these values.
The MSE value measures the mean squared difference between the original and reconstructed values, it provides a general estimation of the reconstruction quality. The lower the MSE value, the closer the reconstructed signal is to the original. Peak signal-to-noise ratio (PSNR) is a metric used to measure the quality of a compressed or reconstructed image by comparing it to the original. It measures the ratio between the maximum possible power of the reconstruction and the power of corrupting noise that affects the fidelity of its representation. It provides a global estimation of the quality of the reconstructed values and an idea of the noise impact. The higher the PSNR value, the more similar the reconstructed values are to the original ones, and thus the better the quality. Structural similarity index measure (SSIM) is a metric used to measure the similarity between two images. The SSIM index ranges from -1 to 1, where a value of 1 indicates perfect similarity between the two images, and a value of -1 indicates complete dissimilarity. The higher the SSIM value, the more similar the images are in terms of structure and texture, and thus the better the quality.

5. Results: Reconstruction of the intervertebral disc's chromophore composition

Reconstructions of the unknown chromophores' composition, *i.e.* values of the collagen r_c and water r_w proportions, were obtained in 3D with known absorption and scattering coefficient spectra of the IVD's elementary constituents (Fig.2). The range of variation of the two unknowns is bounded between 0 and 1 only. The reconstructions were obtained by using synthetic measurements computed at $\lambda_1 = 532$ nm and $\lambda_2 = 960$ nm. Results obtained for the three above-described approaches with $\Gamma = 1$, $\Gamma = \Gamma(r_c, r_w)$ and Γ unknown (ratio of measurements, reference measurement at $\lambda_3 = 560$ nm) are presented without noise added to the data first in Fig. 5. However, it should be noted that intrinsic noise is introduced by the MC simulations. This figure shows a comparison between the reconstructions of r_c and r_w with their ground-truth values. The reconstructions are obtained in 3D, but for the sake of simplicity, only the 2D reconstruction maps of the transverse plane and a 1D cross-section extracted from this one are illustrated. The evolution of the cost function is also shown.

From the reconstructed values of the chromophores' proportions r_c and r_w when Γ is unknown, this one can be calculated from Eq. 11, the results are shown on Fig. 6. The quality of the reconstruction in 3D, assessed through the considered metrics

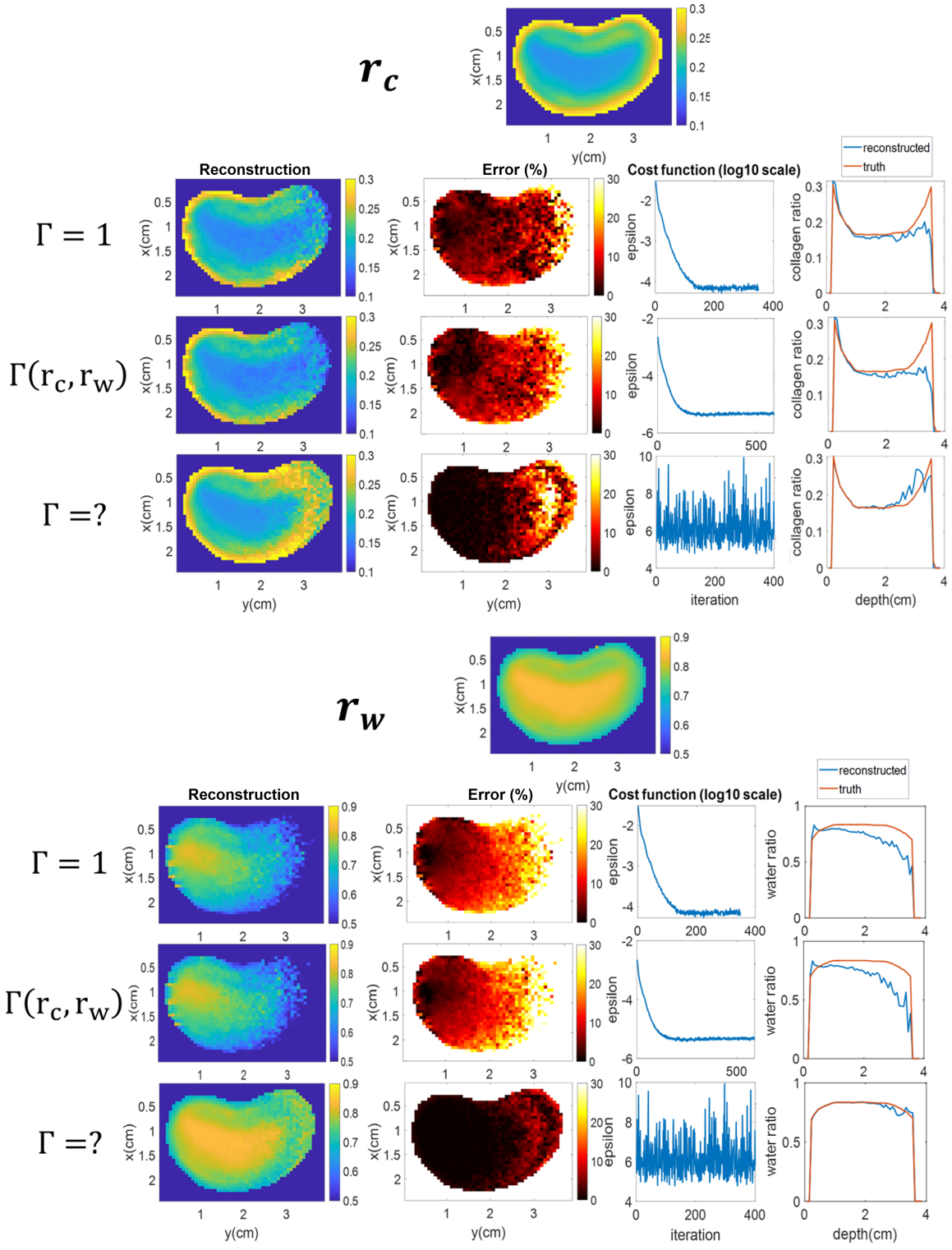

Figure 5. Left, reconstructions in the transverse plane of r_c (top) and r_w (bottom) for $\Gamma = 1, \Gamma(r_c, r_w)$ and unknown Γ (measurement ratios). Middle, Error map (%) and cost function values. Right, 1D cross-section of the reconstructions, x=1 cm. $k_{noise} = 0$, $\tau = 0$.

(Eq.18), is reported in Fig. 7.

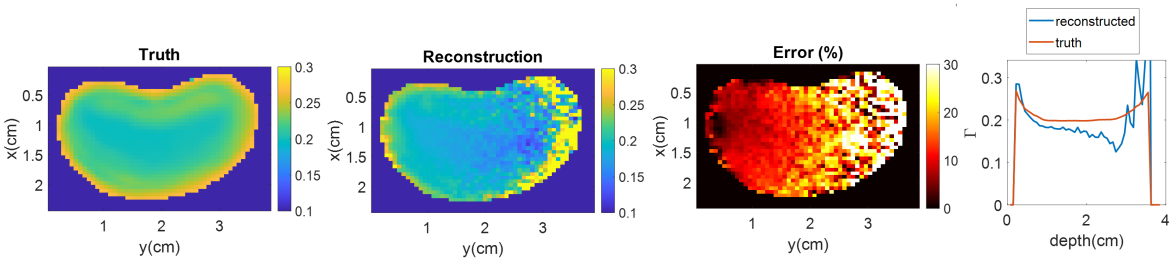

Figure 6. Grüneisen parameter computed from the chromophore concentrations reconstructed with the measurement ratio method. $k_{noise} = 0$, τ=0.

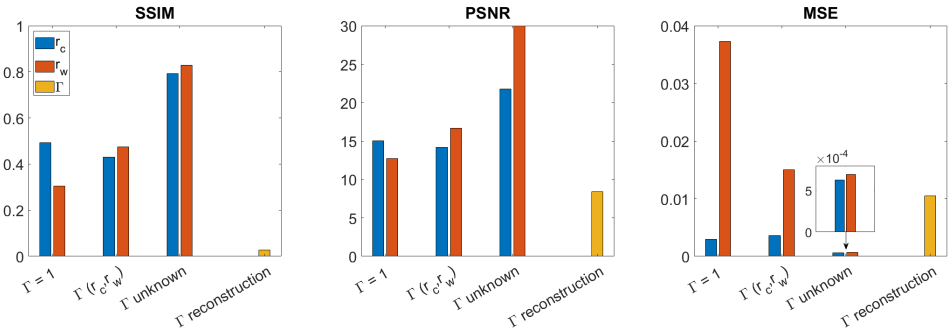

Figure 7. Metrics calculated on the 3D volume of reconstructed values of r_c and r_w for the three considered methods with noiseless measurements and for the calculated Γ when unknown.

As shown in Fig.5, the ratio method provides the best reconstruction of r_c and r_w. However, the cost function associated with this method exhibits erratic behaviour during gradient descent. This instability can be mitigated by selecting an appropriate value for the regularization parameter τ. The impact of introducing this parameter in the cost function of the ratio method is presented in Fig.8.

The effect of noise parameter k_{noise} is illustrated in Fig. 9 for the reconstruction of r_c only; similar reconstructions are obtained for r_w (not shown).

6. Discussion

In all considered scenarios, the results demonstrate excellent reconstructions of the IVD's composition, even when dealing with noisy data, to a depth that is influenced by the level of measurement noise. Notably, superior results are achieved when the Grüneisen parameter is unknown and when ratios of measurements are utilised.

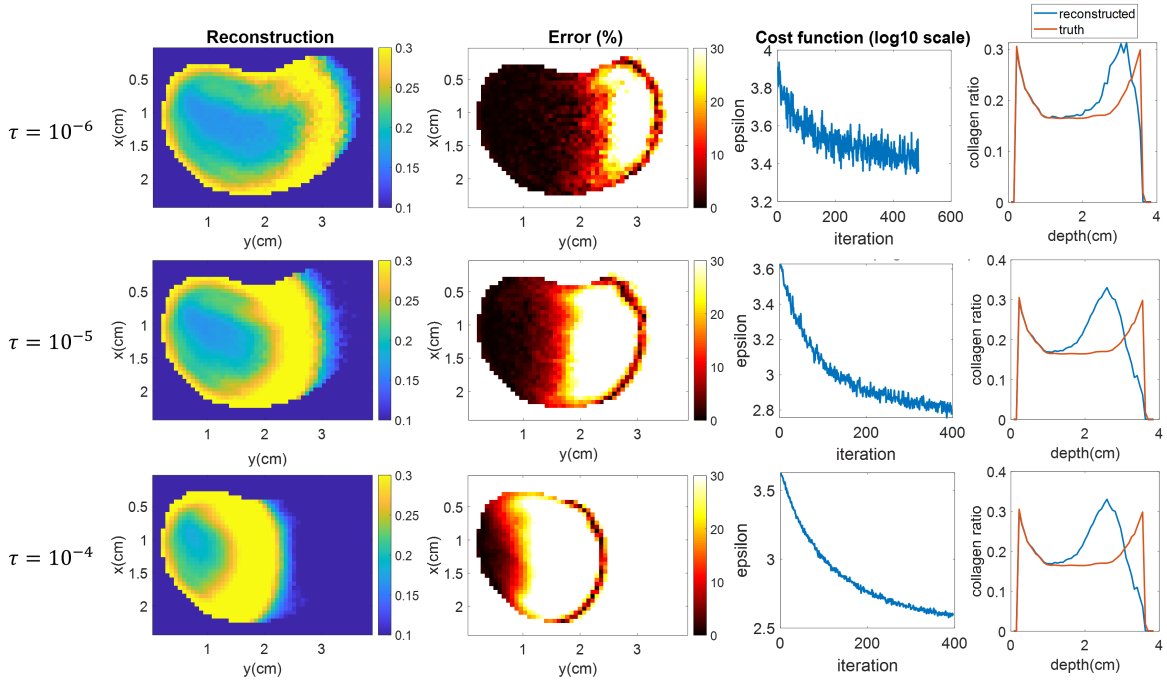

Figure 8. Effect of the τ parameter (ratios method) on the reconstruction of r_c and on the evolution of the cost function with the measurement ratio method. $k_{noise} = 0$. The reconstruction with $\tau = 10^{-6}$ was stopped after 487 iterations.

6.1. Reconstructions of chromophores' proportions with prior knowlegde of the Grüneisen parameter

The results of the reconstruction with noiseless data for the collagen and water proportions are shown on Fig.5 (rows Γ=1 and $\Gamma(r_c, r_w)$) and Fig. 7 highlight the fact that the reconstruction of collagen's proportion appears to outperform that of water's. This is particularly visible in the MSE values, while SSIM and PSNR are roughly similar for both water and collagen. These metrics are calculated over the entire volume of the organ, and locally their values differ significantly. For $y < 2$ cm, the 1D profiles show similar reconstruction errors for both collagen and water, with values below 10%. The reconstruction results obtained when considering the relation of $\Gamma(r_c, r_w)$ (Eq. 12) are similar to those obtained when $\Gamma = 1$. The associated reconstruction errors follow the same trends with values below 10% for $y < 2$ cm. However, knowledge of Γ is a strong prior, currently not well-described in the literature. Therefore, the proposed mixing law to describe the Grüneisen parameter of IVD may not accurately represent the actual relationship. Additional investigations are needed to confidently use this method in the context of the IVD.

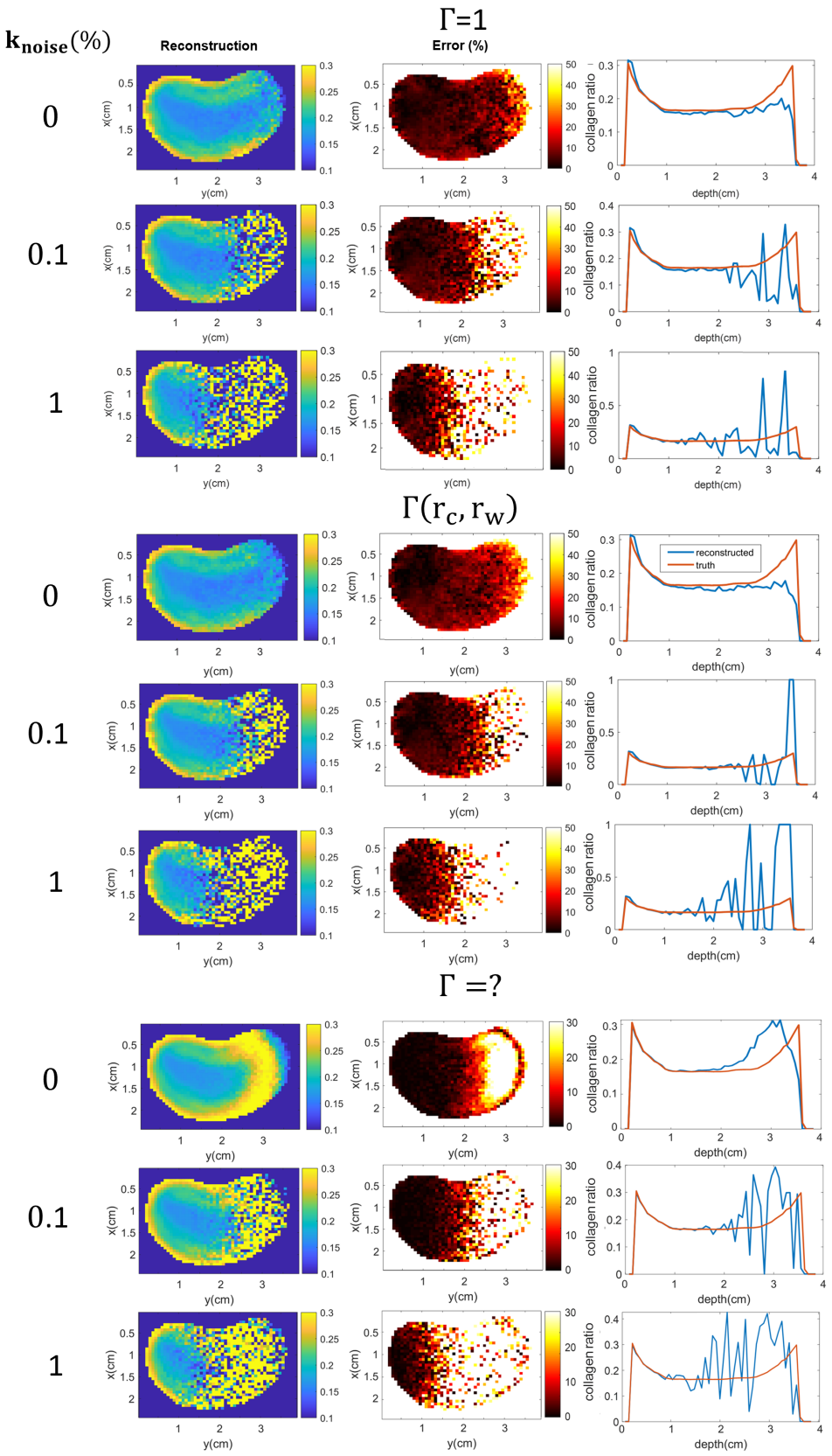

Figure 9. Noise influence on the reconstruction of the collagen proportion for $\Gamma = 1$ (top), $\Gamma(r_c, r_w)$ (middle) and unknown Γ with $\tau = 10^{-6}$ (bottom).

6.2. Reconstructions of the chromophores' proportions and the Grüneisen parameter without prior knowledge

Clearly, the reconstructions obtained by considering normalised measurements (Eq.3) in Fig. 5 (row Γ=?) show higher quality (see Fig. 7), despite the extremely unstable behaviour of the cost function (Fig. 5), when τ=0. Since the cost function is calculated over the entire volume, instability can easily arise, especially in deeper areas, where the variance of the computed fluence is high and where the noise has a greater influence. Consequently, due to the erratic behaviour of the cost function, its value could not be used as the stop criterion and the algorithm had to be manually stopped (here after 400 iterations). This behaviour clearly demonstrates the importance of using the regularization parameter τ to avoid potential division by zero or very small values and to efficiently use the cost function curve to stop the algorithm. This erratic behaviour is primarily due to regions where the noise generated by the MC simulations is high, *i.e.*, deepest regions of the disc where only few photons can reach. Despite this fact, the reconstructions exhibit accurate values for both water and collagen (error is below 5% for both unknowns) up to $y = 1.5$ cm, indicating stable behaviour at the local level in voxels where the signal is strong enough, i.e., near the source. With the reconstructed values of r_c and r_w, Γ can be computed with Eq.12 (Fig. 6). Although the level of accuracy is naturaly degraded, the error stays below 15% for $y < 2$ cm.

6.3. Effect of noise and regularisation parameters

Fig. 9 shows a direct relation with the accessible depth of quantification: higher noise levels result in shallower quantification depths. Introducing a regularisation parameter in the cost function (e.g. L_2) can effectively produce smoother reconstructions without altering the accessible depth of quantification. When Γ is unknown, the introduction of the regularisation parameter τ (Fig.8), even if very small, is conversely fundamental to stabilise the evolution of the cost function.

7. Conclusion

In this preliminary work, we introduce a proof-of-concept QPAI method that avoids the dependence on strong prior knowledge of the Grüneisen coefficient while maintaining a simple illumination strategy. A model-based gradient-descent approach was adopted and the adjoint method was used to compute the gradients derived within the optical inverse problem in QPAI. The forward and adjoint radiative transfer equations were solved with Monte Carlo simulations. Two situations were considered: i) where Γ was supposed to be known *a priori*, eventually, including a law linking $\Gamma(r_c, r_w)$ and the chromophores' proportions; ii) where no prior knowledge was introduced. The quality of the reconstructions obtained demonstrates the feasibility of *in situ* measurements of the IVD's chromophore composition. Furthermore, in the latter case, leveraging multiwavelength measurements, a new reconstruction scheme was proposed

to recover both composition and mechanical information. Ratios of measurements at different wavelengths were considered as the measurements, and the corresponding cost function for minimization was derived accordingly. The approach can be generalized to assess additional chromophores (e.g. proteoglycans, lipids...) by employing sets of measurements at appropriate wavelengths, and is not restricted to the considered organ. A comprehensive literature review on the opto-mechanical properties of the IVD and MRI volume data acquisition of porosity maps allowed the implementation of a highly realistic digital phantom, from which synthetic PA data were generated. Various strategies of PA measurements of the IVD composition in terms of water and collagen content were proposed. Various approaches to reconstruct the three unknown quantities r_c, r_w and Γ throughout the entire volume of the disc were explored, by considering data acquisition geometries compatible with future experimental scenarios. The stability and noise sensitivity demonstrate the robustness of the proposed method that outperforms the conventional one, even without the prior knowledge of Γ. Although the cost function exhibited high instabilities during the minimisation process, the use of the ADAM algorithm allowed for efficient local updates of the unknowns. We also showed that these instabilities could be controlled with the introduction of a regularisation parameter τ and other conventional regularisation strategies can be preferred. In conclusion, this numerical study supports the possibility of using QPAI as a faster, and more flexible, imaging technique, that potentially could be used during surgery within the operating room, to assess the discs' viability, especially those adjacent to the one being operated (by excision, spinal fusion or innovative treatment options). Definitely, a long journey still lies ahead. Experimentally, such device can be obtained by modifying a conventional ultrasound probe by adding pulsed illumination with a tunable laser through optical fibers (e.g.[62]). On the algorithmic side, as for other proposed optical inversion approaches, the first aspect to be addressed is the coupling with the ultrasound propagation model and the handling of inherent artefacts. We believe that the robustness of the proposed approach offers a clear advantage over existing methods. Future developments will therefore include the integration of acoustic propagation modelling, which requires in the organ studied specific adaptations to accurately account for the high impedance mismatch of the lateral vertebrae. On the experimental side, tests on phantoms, specifically designed to mimic the IVD opto-mechanical properties, will be carried out prior to preclinical studies, in order to validate the approach and to guide the design of a dedicated medical device.

Acknowledgments

The authors declare no conflicts of interest.

[1] Lediju Bell M A 2020 *Journal of Applied Physics* **128** 060904
[2] Sun Y, Sobel E and Jiang H 2013 *Journal of Optics* **15** 055302
[3] Wang X, Xie X, Ku G, Wang L V and Stoica G 2006 *Journal of Biomedical Optics* **11** 024015

[4] Laufer J, Elwell C, Delpy D and Beard P 2005 *Physics in Medicine and Biology* **50** 4409–4428
[5] Zhang H F, Maslov K, Sivaramakrishnan M, Stoica G and Wang L V 2007 *Applied Physics Letters* **90** 053901
[6] Oh J T, Li M L, Zhang H F, Maslov K, Stoica G and Wang L V 2006 *Journal of Biomedical Optics* **11** 034032
[7] Jansen K, Van Der Steen A F W, Van Beusekom H M M, Oosterhuis J W and Van Soest G 2011 *Optics Letters* **36** 597
[8] Xu Z, Li C and Wang L V 2010 *Journal of Biomedical Optics* **15** 036019
[9] Attia A B E, Balasundaram G, Moothanchery M, Dinish U, Bi R, Ntziachristos V and Olivo M 2019 *Photoacoustics* **16** 100144
[10] Farooq A, Sabah S, Dhou S, Alsawaftah N and Husseini G 2022 *Nanomaterials* **12** 393
[11] Yuan Z, Zhang Q and Jiang H 2006 *Opt. Express* **14** 6749–6754
[12] Zemp R J 2010 *Appl. Opt.* **49** 3566–3572
[13] Haltmeier M, Neumann L and Rabanser S 2015 *Inverse Problems* **31** 065005
[14] Ding T, Ren K and Vallélian S 2015 *Inverse Problems* **31** 095005
[15] Song N, Deumié C and Silva A D 2014 *Biomed. Opt. Express* **5** 3960–3974
[16] Tian C, Shen K, Dong W, Gao F, Wang K, Li J, Liu S, Feng T, Liu C, Li C, Yang M, Wang S and Tian J 2024 *Photonics Insights* **3** R06
[17] Cox B T, Arridge S R and Beard P C 2009 *J. Opt. Soc. Am. A* **26** 443–455
[18] Tarvainen T and Cox B 2023 *Journal of Biomedical Optics* **29** S11509
[19] Kuchment P and Kunyansky L 2011 Mathematics of Photoacoustic and Thermoacoustic Tomography *Handbook of Mathematical Methods in Imaging* ed Scherzer O (New York, NY: Springer New York) pp 817–865
[20] Hristova Y, Kuchment P and Nguyen L 2008 *Inverse Problems* **24** 055006
[21] Belhachmi Z, Glatz T and Scherzer O 2016 *Inverse Problems* **32** 045005
[22] Bal G and Ren K 2012 *Inverse Problems* **28** 025010
[23] Cox B T, Arridge S R, Köstli K P and Beard P C 2006 *Applied Optics* **45** 1866
[24] Rosenthal A, Razansky D and Ntziachristos V 2009 *IEEE Transactions on Medical Imaging* **28** 1997–2006
[25] Hauptmann A and Cox B T 2020 *Journal of Biomedical Optics* **25**
[26] Yang C, Lan H, Gao F and Gao F 2021 *Photoacoustics* **21** 100215
[27] Yuan Z, Wang Q and Jiang H 2007 *Optics Express* **15** 18076
[28] Cox B T, Arridge S R and Beard P C 2009 *Journal of the Optical Society of America A* **26** 443
[29] Tarvainen T, Pulkkinen A, Cox B T, Kaipio J P and Arridge S R 2013 *IEEE Transactions on Medical Imaging* **32** 2287–2298
[30] Saratoon T, Tarvainen T, Cox B T and Arridge S R 2013 *Inverse Problems* **29** 075006
[31] Hänninen N, Pulkkinen A, Arridge S R and Tarvainen T 2022 *Journal of Biomedical Optics* **27**
[32] Capart A, Wojak J, Allais R, Ghiss M, Boiron O and Da Silva A 2022 *Photonics* **9** 116
[33] Pulkkinen A, Cox B T, Arridge S R, Kaipio J P and Tarvainen T 2014 *Inverse Problems* **30** 065012
[34] Tricoli U, Macdonald C M, Silva A D and Markel V A 2017 *Opt. Lett.* **42** 362
[35] Buchmann J, Kaplan B A, Powell S, Prohaska S and Laufer J 2019 *Journal of Biomedical Optics* **24** 1
[36] Saratoon T, Tarvainen T, Cox B T and Arridge S R 2013 *Inverse Problems* **29**
[37] Antoniou J, Steffen T, Nelson F, Winterbottom N, Hollander A P, Poole R A, Aebi M and Alini M 1996 *Journal of Clinical Investigation* **98** 996–1003
[38] Newell N, Little J, Christou A, Adams M, Adam C and Masouros S 2017 *Journal of the Mechanical Behavior of Biomedical Materials* **69** 420–434
[39] Samanta A, Lufkin T and Kraus P 2023 *Frontiers in Public Health* **11** 1156749
[40] Roughley P J 2004 *Spine* **29** 2691–2699
[41] Eyre D R and Muir H 1977 *Biochimica et Biophysica Acta (BBA) - Protein Structure* **492** 29–42
[42] Metwally K, Boiron O, Deplano V, Prost S and Silva A D 2019 Probing intervertebral discs with

photoacoustics *Opto-Acoustic Methods and Applications in Biophotonics IV* (Optica Publishing Group) p 11077 61

[43] Sekar S K V, Bargigia I, Mora A D, Taroni P, Ruggeri A, Tosi A, Pifferi A and Farina A 2017 *Journal of Biomedical Optics* **22** 015006

[44] Hale G Mand Querry M R 1973 *Applied Optics* **12** 555–563 URL `https://omlc.org/spectra/water/data/hale73.txt`

[45] Jacques S L 2013 *Physics in Medicine Biology* **58** R37

[46] O'Brien W D 1977 *Ultrason. Int. IPC Sci. Technol.* 194–205

[47] Zhutovsky S and Kovler K 2015 Evaluation of the Thermal Expansion Coefficient Using Non-Destructive Testing *CONCREEP 10* (Vienna, Austria: American Society of Civil Engineers) pp 1137–1146

[48] Weir C E 1948 *Journal of Research of the National Bureau of Standards* **41** 279

[49] Wilson W D 1959 *Journal of the Acoustical Society of America* **31** 1067–1072

[50] Foundation I 2022 Tissue Properties Database V4.1 URL `https://itis.swiss/virtual-population/tissue-properties/downloads/database-v4-1/`

[51] Duck F A 1990 *Physical Properties of Tissues : A comprehensive reference book* (Elsevier)

[52] Ur'yash V F, Sevast'yanov V I, Kokurina N Y, Porunova Y V, Perova N V and Faminskaya L A 2006 *Russian Journal of General Chemistry* **76** 1363–1367

[53] Ghiss M, Giannesini B, Tropiano P, Tourki Z and Boiron O 2016 *Computer Methods in Biomechanics and Biomedical Engineering* **19** 1079–1088

[54] Marti D, Aasbjerg R N, Andersen P E and Hansen A K 2018 *Journal of Biomedical Optics* **23** 1

[55] Li C and Wang L V 2009 *Phys. Med. Biol.* **54** R59–R97 ISSN 0031-9155, 1361-6560

[56] Colton D and Kress R 1992 *Inverse Acoustic and Electromagnetic Scattering Theory* (Springer Verlag)

[57] Luke G P, Nam S Y and Emelianov S Y 2013 *Photoacoustics* **1** 36–42

[58] Heino J, Arridge S R, Sikora J and Somersalo E 2003 *Physical Review E* **68** 031908

[59] Hochuli R 2016 *Monte carlo methods in quantitative photoacoustic tomography* Ph.D. thesis University College London

[60] Kingma D P and Ba J 2014 *ARXIV* Publisher: arXiv Version Number: 9 URL `https://arxiv.org/abs/1412.6980`

[61] Wang Z, Bovik A, Sheikh H and Simoncelli E 2004 *IEEE Transactions on Image Processing* **13** 600–612

[62] Zhang J, Arroyo J and Bell M A L 2025 *Biomed. Opt. Express* **16** 995–1005